Research Square

Preprints are preliminary reports that have not undergone peer review.
They should not be considered conclusive, used to inform clinical practice,
or referenced by the media as validated information.

Characterisation of the turbulent solar plasma in the acceleration region of the Sun using BepiColombo radiometric data

Irene Doria

irene.doria@uniroma1.it

Sapienza University of Rome: Universita degli Studi di Roma La Sapienza https://orcid.org/0000-0001-7435-466X

Paolo Cappuccio

SSC Space for ESA/ESAC

Ivan di Stefano

Sapienza University of Rome: Universita degli Studi di Roma La Sapienza

Shota Chiba

Nagoya University: Nagoya Daigaku

Takeshi Imamura

University of Tokyo Graduate School of Frontier Sciences: Tokyo Daigaku Daigakuin Shinryoiki Sosei Kagaku Kenkyuka

Luciano Iess

Sapienza University of Rome: Universita degli Studi di Roma La Sapienza

Research Article

Keywords: BepiColombo, radio science, solar plasma, turbulence, solar wind

Posted Date: November 9th, 2026

DOI: https://doi.org/10.21203/rs.3.rs-11281436/v1

License: This work is licensed under a Creative Commons Attribution 4.0 International License.
Read Full License

Characterisation of the turbulent solar plasma in the acceleration region of the Sun using BepiColombo radiometric data

Irene Doria[1], irene.doria@uniroma1.it

Paolo Cappuccio[2], paolo.cappuccio@ext.esa.int

Ivan di Stefano[1], ivan.distefano@uniroma1.it

Shota Chiba[3], chiba-shota55@nagoya-u.jp

Takeshi Imamura[4], t_imamura@edu.k.u-tokyo.ac.jp

Luciano Iess[1], luciano.iess@uniroma1.it

Affiliations

1. Sapienza University of Rome, Department of Mechanical and Aerospace Engineering (DIMA), Rome, Italy
2. SSC Space for ESA/ESAC, Villafranca Del Castillo, Spain
3. Nagoya University, Institute for Space-Earth Environmental Research, Nagoya, Japan
4. The University of Tokyo, Graduate School of Frontier Sciences, Kashiwa, Chiba, Japan

Corresponding author

Irene Doria, irene.doria@uniroma1.it

Abstract

The acceleration region of the solar wind is still a little-explored region due to its harsh environment a few in situ data are available. In this work, we have studied the characteristics of the turbulent solar plasma using radio science data from BepiColombo solar conjunction experiments. In this configuration the line of sight of the radio signal passes really close to the Sun, and the main noise contribution to the data is the solar plasma. Multi-frequency radio links allow a precise calibration of Doppler and range observables by isolating the plasma contribution, which may then be used to characterise the solar corona. In this study, Doppler and range data from five BepiColombo superior solar conjunctions were analysed: this data set spans different phases of the solar cycle, allowing us to observe the variability of the solar corona due to solar activity. First, the plasma content in the data was characterised through the computation of the power spectral density. A typical regime for the solar wind is that of a well-developed turbulence, so we compared the computed spectra with the expected Kolmogorov behaviour ($f^{-2/3}$ for Doppler observables and $f^{-5/3}$ for range observables). Exploiting the collected open-loop recordings at high frequency (4 kHz),

we fitted the intensity time series to a theoretical model of the spectrum to simultaneously estimate multiple solar wind parameters (amplitude, velocity, axial ratio, inner scale of turbulence, and power law index), characterising the turbulent regime in the vicinity of the Sun (in the range ~ 4-28 solar radii). The results show that the inner scale increases with increasing impact parameter, consistent with theoretical models, while the velocity exhibits a variable behaviour with values on average increasing up to $12R_{\odot}$ and then stabilising around 300-400 km/s.

Keywords

BepiColombo, radio science, solar plasma, turbulence, solar wind.

1 Introduction

Solar wind acceleration and coronal heating remain fundamental problems in solar physics. It is generally accepted that the energy for coronal heating and solar wind acceleration originates from convective motions at the level of the photosphere, which excite magnetohydrodynamic (MHD) waves propagating into the solar atmosphere and

52 the heliosphere (e.g., Cranmer and Winebarger, 2019; Viall and Borovsky, 2020). Two
53 primary scenarios, the wave/turbulence-driven model (e.g. Suzuki & Inutsuka 2005;
54 Cranmer 2012; Shoda et al. 2019) and the interchange magnetic reconnection model
55 (e.g., Bale et al., 2023; Iijima et al., 2023; Raouafi et al., 2023), have been investigated
56 as important scenarios for the solar wind acceleration. In the wave–turbulence–driven
57 scenario, a fraction of outward-propagating Alfvén waves partially reflects in the
58 extended corona, interacts nonlinearly, and generates a turbulent cascade that transfers
59 energy from large to small scales, eventually heating the corona and accelerating the
60 solar wind. In both scenarios, energy transport processes via turbulent cascade play a
61 key role in the outer corona. Hence, determining their spectral properties and radial
62 evolution is essential to understand how energy is transported and dissipated in the
63 corona and in the near-Sun solar wind.
64 Many space missions have investigated the solar corona and solar wind using various
65 techniques. In-situ measurements from missions such as Helios, ACE, Parker Solar
66 Probe (PSP), and Solar Orbiter (SolO) have provided crucial insights into solar wind
67 turbulence at heliocentric distances between ~0.1 and 1 au. However, spacecraft sample

68 solar plasma only locally along their trajectories and have limited access to the critical
69 region very close to the Sun. Missions equipped with high-resolution in-situ plasma
70 instruments, including PSP (e.g., Zank et al., 2021; Raouafi et al., 2023), ACE (e.g.,
71 Stakhiv et al., 2016), and Helios (e.g., Marsch 2012), have further advanced our
72 understanding of heating and acceleration processes. Numerous studies based on L1
73 missions (ACE, WIND) and deep-space probes have also examined solar wind
74 turbulence (e.g., Goldstein & Roberts 1995; references therein).
75 Remote-sensing techniques provide complementary information. Coronagraphs and
76 ultraviolet (UV) imagers offer complementary information to the in-situ measurements.
77 The coronagraph that occults the solar disk (the photosphere) captures the large-scale
78 coronal structure and transient events, such as coronal mass ejection (CME). The Solar
79 and Heliospheric Observatory SOHO (Domingo et al., 1995; Cranmer 2004) has been
80 monitoring the solar corona for these three decades using an onboard coronagraph, the
81 Large Angle and Spectrometric Coronagraph (Brueckner et al., 1995). Instead, UV and
82 X-ray imagers provide information on the characteristic structures in the lower
83 atmosphere. Missions that exploit UV or X-ray instruments are, for example, Hinode

84 (Kosugi et al., 2007; Hara 2018) and Solar Dynamic Observatory (SDO) (Pesnell et al.,
85 2012; Sadykov et al., 2020).
86 Interplanetary scintillation (IPS) exploiting distant natural radio sources has long been
87 used to infer solar wind speeds and turbulence properties from radio-wave scattering in
88 the inner heliosphere (e.g., Scott et al., 1983; Tokumaru et al., 1991). In the IPS
89 measurements, the Very Long Baseline Interferometry (VLBI) stations were also
90 utilised to study the turbulent regime in the solar corona (e.g., Spangler et al., 2002;
91 Sakurai et al., 1992). Coles and Harmon (1989) investigated a radial evolution of the
92 turbulent spectra by using five different techniques. They showed that the dissipation
93 scale of the turbulence monotonically increases with distance. Manoharan and Salter
94 (2025) derived averaged intensity scintillation spectra observed at different frequencies,
95 and the radio sources with shorter wavelength have the larger axial ratio of the plasma
96 density irregularities.
97 A technique closely related to IPS is radio occultation using spacecraft radio signals.
98 The radio occultations have also been exploited to study physical processes in the solar
99 corona. Many missions have conducted solar corona experiments during solar

100 conjunctions, when the radio signal passes close to the Sun, with the spacecraft
101 positioned on the far side relative to Earth, offering valuable opportunities to investigate
102 the solar corona (Figure 1). Some notable missions that have conducted these types of
103 observations include Viking (Tyler et al., 1977), Galileo (Efimov et al., 2005), and
104 Akatsuki (Imamura et al., 2014). Imamura et al. (2005) demonstrated that the phase
105 scintillation spectra were not represented by a single power law, displaying a
106 Kolmogorov-like slope at low frequency (wave number), a local flattening near ~0.5–3
107 Hz (600–100 km), and a steepening at high frequencies, where dissipation becomes
108 important. Other missions that have been exploited for solar studies using radio links
109 are Cassini (Richie-Halford et al. 2009) and BepiColombo (Cappuccio et al., 2024).
110 Thanks to the multifrequency radio link configuration enabled by X- and Ka-band
111 transponders (Bertotti et al., 2003; Iess et al., 2021), plasma noise can be singled out
112 and removed, leading to better accuracies in the measurements.
113 BepiColombo, a joint mission between the European Space Agency (ESA) and the
114 Japanese Space Agency (JAXA) launched on 20th October 2018 (Benkhoff et al., 2021),
115 hosts the Mercury Orbiter Radio-science Experiment (MORE), which performs multi-

116 frequency range and Doppler measurements through three downlink and two uplink
117 microwave signals in X- and Ka-band (Iess et al., 2021). MORE performs superior solar
118 conjunction experiments to test general relativity and alternative theories of gravity. The
119 combination of X- and Ka-band links allows precise calibration of plasma effects due to
120 solar corona in both Doppler and range measurements (Bertotti et al., 1993; Bertotti et
121 al., 2003; Iess et al., 2021). In addition to closed-loop data, high signal-to-noise open-
122 loop recordings provide intensity time series suitable for scintillation and spectral
123 analyses, enabling the study of turbulence over a wide range of spatial scales.
124 This study presents the first comprehensive characterisation of solar wind turbulence in
125 the range 4–28 solar radii using multi-mode, multi-frequency radiometric data acquired
126 during five BepiColombo superior solar conjunction experiments. Section 2 reports a
127 brief description of the solar conjunction experiment, the observations geometry, the
128 BepiColombo radio-tracking system, and the method used for plasma calibrations. In
129 Section 3, we analyse closed-loop Doppler and range data to examine the spectral
130 properties of phase fluctuations and assess their consistency with Kolmogorov
131 turbulence. In Section 4 we use open-loop intensity spectra to estimate key physical

132 parameters of the turbulent plasma, including solar wind speed and the inner scale of
133 turbulence, and to investigate their radial evolution in the corona and the near-Sun solar
134 wind. Finally, Section 5 summarises the results of these analyses.
135
136 **Figure 1** Geometry of a superior solar conjunction where the Sun (S) is between the
137 probe (P) and the Earth (E). The letter b indicates the impact parameter of the radio link.
138

139 2 Observations

140 Observations were conducted using radiometric measurements from BepiColombo's
141 radio science system when the spacecraft passed on the opposite side of the Sun as seen
142 from the Earth (superior conjunction). The configuration of a superior solar conjunction
143 is characterised by two angles: the Sun-Probe-Earth angle (SPE) and the Sun-Earth-
144 Probe angle (SEP). The SEP is used to identify superior solar conjunctions when the
145 spacecraft is in an orbit beyond the Earth. The SPE is used to identify the superior solar
146 conjunctions when the spacecraft is in the inner Solar System, that is the case of
147 BepiColombo.

In this study, we analyse radiometric data from five Solar Conjunction Experiments (SCE) carried out during the cruise phase of BepiColombo. The impact parameter (defined as the shortest distance between the centre of the Sun and the line of sight - b in Figure 1), ranges from about 4 to 28 solar radii (see Table 1), and the observations were carried in the southern hemisphere of the Sun for all the experiments except for SCE5 that covered the northern hemisphere. The SCEs span from 2021 (close to a solar minimum) to the end of 2023 (in the ascending phase of the solar cycle, towards a solar maximum). The dates for each experiment together with the impact parameter and the heliolatitude range are reported in Table 1. The geometries of these five experiments are reported in Figure 2.

Table 1 BepiColombo solar conjunction experiments during cruise phase.

SCE	**Start**	**End**	**Impact parameter ($R_\odot$)**	**Heliolatitude (deg)**
SCE1	10th March 2021	24th March 2021	$4.3 - 18.5$	$(-13.4°) - (-79.3°)$
SCE2	29th January 2022	12th February 2022	$7.7 - 24.0$	$(-15.3°) - (-82.4°)$
SCE4	29th January 2023	12th February 2023	$8.1 - 21.6$	$(-17.7°) - (-82.0°)$
SCE5	26th June 2023	6th July 2023	$4.0 - 28.3$	$5.6° - 87.8°$
SCE6	8th December 2023	22nd December 2023	$4.6 - 10.3$	$(-14.6°) - (-85.1°)$

160 **Figure 2** Geometry of BepiColombo superior solar conjunctions. The markers indicate
161 the position of the probe at the middle of a tracking pass in the plane orthogonal to the
162 ray path as seen from the Earth. BepiColombo is moving in the direction shown by the
163 arrows.
164
165 Figure 3 shows EUV (extreme-ultraviolet) images of the Sun taken by the AIA
166 (Atmospheric Imaging Assembly) instrument (Lemen et al., 2012) onboard the SDO
167 (Solar Dynamics Observatory) mission during the five solar conjunction experiments.
168 Figure 3a-c, in particular, shows the Sun during SCE1: it can be noticed that the Sun is
169 less active compared to the other images since we are close to a solar minimum;
170 moreover, a coronal hole is present in the south pole, so the central passes of SCE1 are
171 likely to have probed fast solar wind. A small coronal hole seems to be present in the
172 south pole also in Figure 3f (during SCE2) and Figure 3g (during SCE4), so
173 BepiColombo may have probed fast solar wind during the central passes of these other
174 solar conjunctions. Looking at Figure 3j-o, it seems that no other coronal holes are
175 present close to the regions probed by BepiColombo; this is due also to the fact that

176 close to a solar maximum the number of coronal holes decreases as the Sun becomes
177 more active.
178
179 **Figure 3** EUV images of the Sun at a wavelength of 193 Å acquired by SDO/AIA
180 (http://jsoc.stanford.edu). Each row shows images for a different SCE: a-c) SCE1, d-f)
181 SCE2, g-i) SCE4, j-l) SCE5, and m-o) SCE6. The three images for each row (from left
182 to right) represent the Sun at the beginning, at the centre and at the end of the
183 conjunction experiment.
184
185 **2.1 Radio-tracking system**
186 The BepiColombo radio system is equipped with a multi-frequency link, where two
187 uplink carriers and three downlink carriers in X- and Ka-band are simultaneously used.
188 The Ka-band transponder (KaT) receives a Ka-band uplink signal (at 34.4 GHz) and
189 retransmits it coherently to the ground at Ka-band (32.1 GHz); the Deep Space
190 Transponder (DST) allows for a X-band uplink carrier (at 7.2 GHz) coherent with a X-
191 band downlink (8.4 GHz) and a Ka-band downlink (32.0 GHz). The configuration

192 scheme is reported in Figure 4.

193 Doppler and range measurements will be carried out whenever the radio link will be

194 established. In order to track a spacecraft signal carrier, the closed-loop receiver utilises

195 a phase locked loop (PLL) that precisely measures and records the carrier's phase. In

196 open-loop reception, an independent broad band receiver is used without the PLL

197 tracking mechanism; the receiver down-converts the spacecraft signal via a local

198 oscillator heterodyne process guided by a prediction of the expected frequency (Iess et

199 al., 2021). From the open-loop recordings the intensity of the signal has been extracted

200 (i.e., the intensity of the electric field that arrives at the ground station).

201

202 **Figure 4** The scheme represents the configuration of the BepiColombo on board radio

203 system. The Ka/Ka link is established by the KaT, while the DST establishes the X/X

204 and X/Ka links.

205

206 The primary ground antenna for MORE is the ESTRACK DSA 3 located in Malargue,

207 Argentina. DSA 3 is equipped with X and Ka band transmitters and receivers (Iess et

al., 2021) and with a water vapor radiometer for wet tropospheric delay calibrations (Lasagni Manghi et al., 2023).

2.2 Plasma calibrations

Thanks to the equipped radio-tracking system, we are able to almost completely isolate the plasma signal from the Doppler and range measurements because of its dispersive nature. In fact, the refractive index of plasmas n at microwave frequencies differs from unity by an amount inversely proportional to the square of the carrier frequency f_c (Bertotti and Giampieri, 1998):

$$n \sim 1 - \frac{1}{2}\left(\frac{f_p}{f_c}\right)^2 \qquad (1)$$

with f_p the plasma frequency, which depends on the plasma density N_e as $f_p^2 = \frac{N_e e^2}{4\pi^2 m_e \epsilon_0}$ (e.g., Withers 2010), where e is the electron charge, m_e is the electron mass and ϵ_0 is the permittivity in free space.

In the case of BepiColombo, three observable quantities are available, $y_{X/X}^{obs}$, $y_{X/Ka}^{obs}$ and $y_{Ka/Ka}^{obs}$, one for each link, where *y* can represent the path delay variation or the relative frequency shift. These measurements are combined in a system of three equations in three unknowns, that are the non-dispersive path delay variation or relative

frequency shift y_{nd}, and the contributions from the uplink and downlink plasma at a reference frequency, y_{pl_up} and y_{pl_dn} (Bertotti et al., 1993; Tortora et al., 2004). The system can be solved straightforwardly to find y_{nd}, y_{pl_up} and y_{pl_dn}. In this work the focus is on the analysis of the signal due to plasma, so the quantities y_{pl_up} and y_{pl_dn} will be used.

3 Spectral analysis of the plasma content

3.1 Methodology and turbulence spectra

A Kolmogorov spectrum is expected to well describe the solar wind turbulent flow (Woo and Armstrong, 1979). Under the assumption of incompressibility, the Doppler signal is expected to show a slope of -2/3. This value is derived from the typical Kolmogorov three-dimensional power-law index of the electron density spectrum, which is equal to -11/3. Since the range signal can be interpreted as the integral of the Doppler, its power spectral density (PSD) is expected to follow a slope of -5/3.

A fast Fourier transform algorithm yields a noisy estimate of the power spectrum at high frequencies due to thermal noise. To reduce the variance of the spectrum estimator, we applied a filtering technique based on the Welch method for the computation of the

240 PSD (Stoica and Moses, 2005). This method requires a subdivision of the data sequence
241 in segments, each of which undergoes an operation of windowing; afterwards, for each
242 segment the periodogram is computed. Finally, the PSD is obtained calculating the
243 mean of these periodograms. The chosen shape for the window is the Hanning one. For
244 the Doppler and range observables, two different window lengths of 1800 s and 3600 s
245 have been selected, respectively. These lengths have been selected as a trade-off to
246 minimise thermal noise contribution at high frequencies while maintaining sufficient
247 information content at low frequencies. Since the Doppler time series is sampled at 1
248 second and the range data at 2 seconds, in order to have an equal number of samples per
249 window, the length for the range is twice that of the Doppler.

250 **3.2 Results**

251 Figure 5 reports an example of the PSD for the Doppler and range downlink data
252 obtained on 4th February 2022. The green line represents the expected Kolmogorov
253 slope (Woo and Armstrong, 1979), the blue line reports the observed spectrum, and the
254 red line represents the estimated slope. This estimation has been performed through a
255 least square fitting of the spectra with the function Af^p, where p is the spectral index

256 of interest in this analysis. Figures 6 and 7 show the observed Doppler and range

257 spectra, respectively, for all the conjunctions.

258 To estimate p, it is essential to select the appropriate interval of frequencies where the

259 PSD follows the Kolmogorov spectrum. The spectra present a flattening at higher

260 frequencies, indicating the thermal noise. Although the turbulent spectrum steeply

261 decreases at high frequencies, which is associated with the so-called inner scale

262 indicating dissipations of turbulence, thermal noise prevents a clear appearance of this

263 structure on the range and Doppler PSDs. A method to estimate this parameter will be

264 presented in Section 4. For each pass, the selected frequency intervals are $10^{-3} -$

265 $10^{-1}\ Hz$ for the Doppler measurements and $10^{-4} - 10^{-2}\ Hz$ for the range

266 measurements.

267 The retrieved spectral indices and their uncertainties are shown in Figure 8 and 9 for the

268 Doppler and range data, respectively; the error bars indicate the uncertainties obtained

269 from the fitting procedure. In Figure 9, the variance of the range indices is larger than

270 that of the Doppler indices. The mean Doppler spectral index is about -0.68 and the

271 standard deviation is ~0.09, while the mean range index is about -1.73 and the standard

deviation is ~0.52.

The obtained spectral indices are generally close to those predicted by the Kolmogorov power law for both Doppler and range datasets (Figures 6 and 7). Most of the slopes in Figure 6 are similar in the same solar conjunction except for SCE4 (Figure 6 (c)). On the other hand, the slopes in Figures 7 (a), (c), and (d) show larger deviations than those in Figures 6, meaning that the range data are more sensitive to the solar wind conditions. For SCE6, data from DOY 349 to DOY 354 were excluded because strong scintillation was observed on the X/X link, rendering the data unreliable (see Section 4.1).

Although the Doppler indices do not show the radial dependence in Figure 8, the range indices with larger impact parameters in Figure 9 tend to be flatter, especially beyond 18 solar radii, while within 13 solar radii, most of the range spectra were steeper than the Kolmogorov spectrum. The different trend of the range indices with respect to the Doppler ones may be explained by the higher contribution of thermal noise on the observables; in fact, for range data at large distances from the Sun less plasma is crossed by the signal and the thermal noise dominates over the plasma noise making the

288 spectrum flatter.

289 The trend of the Doppler and range indices also varies from each SCE. In the Doppler
290 data, SCE1, SCE2, and SCE5 mostly follow the Kolmogorov, while most of SCE4 data
291 were steeper than the Kolmogorov, and SCE6 had a large variance. For the range data,
292 most of the spectra were steeper than the Kolmogorov spectrum within 13 solar radii, as
293 mentioned above. Beyond 13 solar radii, SCE1, SCE2, and SCE4 had a large variance,
294 and the indices during SCE5 were flatter than the Kolmogorov.

295

296 **Figure 5** 4th February 2022 PSD Doppler (top) and range (bottom) downlink. Impact
297 parameter was 7.7 solar radii.

298

299 **Figure 6** Observed PSD from Doppler downlink data for all five conjunctions. (a)
300 SCE1, (b) SCE2, (c) SCE4, (d) SCE5 and (e) SCE6. The black dashed line indicates the
301 theoretical Kolmogorov slope.

302

303 **Figure 7** Observed PSD from range downlink data for all five conjunctions. (a) SCE1,

(b) SCE2, (c) SCE4, (d) SCE5 and (e) SCE6. The black dashed line indicates the Kolmogorov slope.

Figure 8 Doppler power-law indices for SCE1, SCE2, SCE4, SCE5 and SCE6. Each point represents a tracking pass. Each observational campaign is represented by a different color, and the dashed line shows the theoretical value of the Kolmogorov spectrum.

Figure 9 Range power-law indices for SCE1, SCE2, SCE4, SCE5 and SCE6. The styles are the same as those in Figure 8.

4 Characterisation of intensity spectra

Intensity time series recorded in the open-loop system can be used to infer physical properties of the turbulent solar plasma. In particular, these data enable estimation of the solar-wind speed and the spatial structures of the turbulence, such as the power-law index of the turbulence spectrum and the inner scale, the lower limit of the inertial range

over which we observe a Kolmogorov-like behaviour.

4.1 Scintillation index

The inner solar corona and the near-Sun solar wind constitute a highly inhomogeneous plasma medium, where strong density fluctuations and turbulence induce intensity scintillation in received radio signals (e.g., Ho 2010). The strength of these scintillations can be quantified through the scintillation index, m. The scintillation index is computed using the open-loop data. Specifically, from these data the phasor's component, I and Q, are extracted, then the amplitude of the signal is computed as:

$$A = \sqrt{I^2 + Q^2} \qquad (2)$$

From Eq. (2) one can derive the intensity:

$$I = A^2$$

Then the scintillation index is defined as a normalised standard deviation of the intensity (Fremouw et al., 1978; Priyadarshi 2015):

$$S4 = \frac{\sqrt{\overline{(I^2)} - (\bar{I})^2}}{\bar{I}} \qquad (3)$$

For this analysis the average intervals have been chosen to have length 0.01 seconds. In order to assess if the X/X link went into strong scintillation one can look at the percentage of points during a pass where the scintillation index is above 1. Two

337 examples are represented in Figure 10: on the left a pass where no strong scintillation is
338 observed and on the right a pass where strong scintillation is observed. The results for
339 the solar conjunctions as function of the impact parameter are shown in Figure 11,
340 where also the solar cycle dependence is outlined.
341
342 **Figure 10** Scintillation index for two passes from SCE6: on the left the pass of 8th
343 December (no strong scintillation) and on the right the pass of 16th December 2023
344 (strong scintillation is observed).
345
346 **Figure 11** Percentage of points with scintillation index above 1 during each pass of the
347 conjunctions as a function of the impact parameter. The colour scale indicates the
348 dependence on the solar cycle (as years after solar minimum).
349
350 ### 4.2 Turbulence spectra and fitting procedure
351 The radio wave that crosses the solar corona is scattered passing through the solar wind
352 by density fluctuations and produces a diffraction pattern at the Earth. This pattern is

353 convected past the observer at the solar wind velocity and is observed as intensity
354 scintillation (Scott et al., 1983). Therefore, the intensity scintillation spectrum reflects
355 the spatial structure of the coronal plasma and the solar wind velocity. The solar wind is
356 thought to involve well-developed turbulence, and the spatial spectrum of the plasma
357 density is expected to approximately follow the Kolmogorov spectrum in the inertial
358 subrange. The turbulence dissipates at the inner scale where the kinetic energy is
359 converted to heat. In the weak scattering regime, the effect of the medium on the radio
360 wave can be represented by a thin phase modulator located at the point of closest
361 approach to the Sun. Besides these assumptions, the weak scattering approximation is
362 assumed. The model density spectrum is chosen to be spherically symmetric $\Phi_n \propto$
363 $R^{-\beta}$, where R is the closest approach distance. Moreover, $\Phi_n(k)$ has a power law
364 form, $\Phi_n \sim k^{-\alpha}$, where k is the wavevector and the exponent α may vary slowly with
365 k (Scott et al., 1983).
366 Hence, a suitable model for the intensity scintillation spectrum is the following (Scott et
367 al., 1983):
368 $$P(f) = \frac{2\pi(\lambda r_e)^2}{V} \int_{-\infty}^{+\infty} \Phi_n\left(k_x = \frac{2\pi}{V} f, k_y\right) F_{diff}(k) dk_y \qquad (4)$$

where V is the flow velocity, f is the temporal frequency of the fluctuations, λ is the wavelength of the received radio signal, r_e is the classical electron radius, k_x is the wavenumber in the radial direction and k_y is the wavenumber in the direction perpendicular to the radial direction and the ray path. The term $F_{diff}(k)$ in Eq. (4) represents the Fresnel propagation filter, which has a high pass form blocking wavenumbers below $k_F = \pi/(\lambda z)^{1/2}$ and it is expressed as follows:

$$F_{diff}(k) = 4\sin^2\left(k^2\frac{\lambda z}{4\pi}\right)$$

where $k = \sqrt{k_x^2 + k_y^2}$ and $z = L_1L_2/(L_1 + L_2)$ with L_1 being the spacecraft-closest approach distance and L_2 being the closest approach-receiver distance. Then the spatial spectrum of the plasma density Φ_n is formulated in the following way:

$$\Phi_n(k) = A\left(\sqrt{k_x^2 + \frac{k_y^2}{AR^2}}\right)^{-\alpha}\exp\left(-\frac{k^2}{k_c^2}\right)R^{-4}$$

where A is a constant, AR is the axial ratio of irregularities that indicates the anisotropy of the density inhomogeneity, α is the power-law exponent of the turbulence spectrum, and k_c is the wavenumber beyond which the turbulence starts to dissipate and that is related to the inner scale S_i as $S_i = 3/k_c$.

This theoretical model can be used to fit the observed data and retrieve the following

parameters: A, AR, α, k_c (or S_i) and V. The fitting procedure is done using the intensity time series retrieved from the open-loop data which represent the intensity of the signal measured at the receiver station (that is the intensity of the electric field that arrives at ground). We excluded data from passes where the X/X link went into strong scintillation; this has been verified through the computation of the scintillation index (see Section 4.1). We also excluded some passes where we observed that the shape of the spectrum could not be well described with the theoretical model presented above; this could be due to problems in data acquisition or to solar corona conditions.

The intensity time series are divided by their mean intensity value, then the PSDs are computed with the Welch method, as seen in Section 3. From the graphs of the spectra a noise floor is evident at frequencies higher than $10^1 - 10^2\ Hz$; the noise level has been estimated computing the mean power in this noise floor. To see the inner scale more clearly, the noise floor was subtracted from the whole spectrum. Finally, the spectrum is smoothed using a moving average technique with a window of size 100 points.

The fitting procedure is performed with a least squares method on a logarithmic scale. Since a high dependence on the initial conditions has been observed, a particle swarm

401 optimisation (PSO) algorithm (Eberhart and Kennedy, 1995; Kennedy and Eberhart,
402 1995) is first performed in order to find the global minimum; its output is then given as
403 input to the least squares fitting. The weights for the least square fitting are computed as
404 the standard deviation of the difference between the data and the model resulting from
405 the PSO.

406 ### 4.3 Results

407 As an example, the results of the spectrum and the solar wind parameters are shown in
408 Figure 12 for the 3rd February 2023. One can observe that there is a good match
409 between the intensity spectrum from the data and the theoretical model. The spectrum
410 presents a flattening at low frequencies, the Fresnel knee round 0.3 Hz, a power-law
411 part related to the inertial subrange and a steepening at high frequencies that indicates
412 the inner scale. These characteristics are well-represented by the fitted theoretical
413 model.

414

415 **Figure 12** Result from the fitting procedure for the intensity spectrum of 3 February
416 2023. The green line is the (averaged) observed spectrum, while the black line is the

417 spectrum from the fitting procedure.

418

419 Here the uncertainties together with the estimated parameters are reported:

420 $$A = (3.11 \pm 1.61) \cdot 10^{67}$$

421 $$V = 381.64 \pm 3.40 \text{ km/s}$$

422 $$S_i = 3.85 \pm 1.04 \text{ km}$$

423 $$AR = 8.33 \pm 1.26$$

424 $$\sigma_\alpha = 2.23 \pm 1.78 \cdot 10^{-1}$$

425 Focusing on the solar wind velocity V and the inner scale of turbulence S_i, we observe
426 that these parameters are estimated with good accuracy. The uncertainty in the velocity
427 is on average ~1.5% of the central value, while for the inner scale, excluding two
428 outliers, the uncertainties are on average 25% of the central value. The resulting solar
429 wind parameters for all the passes are reported as a function of the impact parameter in
430 Figure 13 together with their uncertainties.
431 The values obtained for the plasma velocity increase on average with the impact
432 parameter until ~$12R_\odot$: this is consistent with the fact that in this range of impact

parameters lies the acceleration region, where the solar wind is accelerated; after $12R_{\odot}$ the plasma velocity stabilises around 300-400 km/s. From EUV images in Figure 3, we observed that during SCE1 there was a prominent coronal hole in the south pole, so the passes with impact parameter below 8 $R_{\odot}$ may have probed fast solar wind; in fact, in these range of distances the solar wind was estimated to have velocities around 400 km/s, higher than some of the estimated values for SCE5 and SCE6. Moreover, on 16 March 2021 (SCE1), when the impact parameter was ~$5.4R_{\odot}$, a CME has been detected. These velocities are not as high as typical fast solar wind velocity (~700-800 km/s), but at these impact parameters the solar wind is still accelerating. During the other passes and conjunctions BepiColombo seems to have probed slow solar wind. A big CME was observed also on 9 February 2023 during SCE4 at ~$14R_{\odot}$: on this pass, in fact, we estimated a higher velocity of ~450 km/s with respect to the other passes of the conjunction.

The inner scale of turbulence indicates the limit below which the plasma can no longer maintain its properties as a fluid, the dissipative phenomena become important, and the Kolmogorov spectrum is no longer valid. The results obtained from the intensity spectra

estimation can be compared with a theoretical model, the proton inertial length model (Coles and Harmon, 1989; Chiba et al., 2022), which relates the inner scale to the cyclotron damping of Alfvénic turbulence:

$$S_i = 3\frac{V_A}{\omega_c} = 684\frac{1}{\sqrt{N_e}}km \qquad (5)$$

where V_A is the Alfvén velocity, ω_c is the proton cyclotron frequency, and N_e is the plasma density expressed in cm^{-3}, for which the model by Doria et al. (submitted) is considered:

$$N_e = 1.298 \cdot 10^{12}\left(\frac{R_\odot}{r}\right)^{2.28} e^-/m^3 \qquad (6)$$

The proton inertial length model states that the inner scale is larger for lower densities; moreover, the plasma density decreases with distance, so the inner scale increases.

Then, another theoretical model for the inner scale has been considered, the proton-gyroradius model (Raja et al., 2019; Chiba et al., 2022):

$$S_i = \frac{\mu v_{th}}{eB} = \frac{102\sqrt{\mu T_i}}{B}\ cm \qquad (7)$$

where μ is the ratio between the ion and the proton mass (taken equal to 1), e is the elementary charge, T_i is the proton temperature in eV, and B is the magnetic field in G. This model relates the inner scale to the gyroradius of protons moving at the thermal

velocity: when the temperature of the solar wind increases or the magnetic field is weaker, the inner scale is larger. The ion temperature is considered equal to $10^6 K$, while for the magnetic field the model by Dulk and McLean (1978) is considered:

$$B = 0.5\left(\frac{r}{R_\odot} - 1\right)^{-1.5} \text{ G} \quad (8)$$

From Eq. (8) it is possible to notice that the magnetic field tends to decrease with distance, indicating that, as expected, the inner scale will increase with the distance from the Sun.

The comparison between data and theoretical models (Eqs. (5) and (7)) is reported in the bottom left panel of Figure 13. The data are closer to the proton inertial length model (solid black line), while the proton-gyroradius model (dashed black line) presents lower values with respect to the observed inner scales. There is one main outlier whose value is close to zero; however, it has a large uncertainty and the bar corresponding to the standard deviation crosses the model curve, so the value is statistically compatible with the proton inertial length profile.

As shown in the top right panel of Figure 13, the uncertainties on the axial ratio can be very high, thus this parameter can't be well constrained and estimated.

481 Regarding the results for the power spectral index (bottom right panel of Figure 13), we
482 can see that the values slightly increase with the impact parameter and that below 10
483 $R_\odot$ the values are below the typical Kolmogorov index of 11/3. This may indicate that
484 at very low impact parameters the turbulence may be not yet well-developed. The
485 obtained values are in line with those from Scott et al. (1983); in fact, here it is shown
486 that for values of the impact parameter below 10 $R_\odot$ the spectral index is in general in
487 the interval 2.0-3.0.
488 Finally, it can be noted that the results for impact parameters larger than 20 $R_\odot$ present
489 a different behaviour with respect to smaller radial distances. This may be explained by
490 the fact that in the open-loop data, besides the plasma, other types of noise are present:
491 at large distances, where the plasma content is low, these noises affect the shape of the
492 spectrum, and the model we use may not be valid anymore.
493
494 **Figure 13** Solar wind parameters retrieved from intensity spectra estimation as
495 functions of impact parameter. In the bottom left panel, the solid black curve (proton
496 inertial length model) is referred to Eq. (5), while the dashed black curve (proton

497 gyroradius model) is referred to Eq. (7).

498

499 ## 5 Conclusions

500 The aim of this work is to perform solar wind and solar corona analysis using Doppler
501 and range measurements from the solar conjunction experiments of BepiColombo. In
502 particular, these analyses help to characterise the turbulent regime of the solar plasma
503 and the solar wind in the acceleration region by estimating the power spectral index
504 (compared against the Kolmogorov expected value), the solar wind velocity and the
505 inner scale of turbulence as a function of the radial distance from the Sun.
506 In this work we have used the PSD of closed-loop Doppler and range data to
507 characterise the plasma content in otherwise inaccessible regions and compared the
508 results with the expected spectrum of a turbulent flow. In particular, the power indices
509 have been retrieved for 71 tracking passes: we found values close to the Kolmogorov
510 index (indicating a well-developed turbulence), even though some spread is observed.
511 The mean values are -0.68 for Doppler and -1.73 for range, with standard deviations
512 equal to ~0.09 and ~0.52 respectively.

513 The open-loop data were used to retrieve intensity spectra, which were then fitted with a
514 theoretical model to estimate solar wind parameters, in particular the solar wind velocity
515 and the inner scale of turbulence. The retrieved uncertainties allow a reliable estimation
516 for the parameters of interest (except for the axial ratio). The estimated plasma velocity
517 increases on average until around 12 $R_{\odot}$, which corresponds to the acceleration region,
518 then stabilises near 300-400 km/s, in line with previous analyses of the solar wind speed
519 (Marsden 1996; Imamura et al., 2014). The results obtained for the inner scale show that
520 it increases with the impact parameter, which is consistent with the proton inertial
521 length model (Coles and Harmon, 1989; Chiba et al., 2022). These results should be
522 compared with those obtained using different methods and data sets to delineate more
523 precise radial profiles for the solar wind speed and the inner scale. For example, an
524 alternative method to estimate the solar wind velocity exploiting two spacecraft is
525 presented in Cappuccio et al. (2024), leading to results compatible with those presented
526 in this analysis.
527 Finally, it can be inferred that radio link technique can be exploited for turbulent solar
528 plasma analyses in the proximity of the signal exchanged between the spacecraft and the

Earth. The results that we obtained can be then compared with other missions' data (e.g. Parker Solar Probe, Solar Orbiter and Akatsuki) to have a more precise view of the turbulent processes in the acceleration region of the solar wind.

Declarations

Ethics approval and consent to participate

Not applicable

Consent for publication

Not applicable

Availability of data and materials

BepiColombo MORE data will be made available through the official ESA Planetary Science Archive (PSA), accessible at http://psa.esa.int (Besse et al., 2018). The calibrated plasma data used in this study are presently available on Zenodo at https://doi.org/10.5281/zenodo.17813314 (Doria et al., 2025), ensuring immediate accessibility.

Competing interests

The authors declare that they have no competing interests.

Funding

This work has been supported in part by the Italian Space Agency under agreement No. 2022-16-HH.1-2024

Authors' contributions

ID and PC together with SC and TI defined the problem and the analysis methodology, ID performed the analysis, then ID, PC, SC, IdS and TI wrote the paper. LI is the PI of the MORE instrument: he provided the data and supervised the work.

Acknowledgements

Not applicable

References

- Bale, S.D., Drake, J.F., McManus, M.D., Desai, M.I., Badman, S.T., Larson,

561 D.E., ... and Kasper, J.C. (2023) Interchange reconnection as the source of the
562 fast solar wind within coronal holes. Nature, 618 (7964), 252-256,
563 https://doi.org/10.1038/s41586-023-05955-3
564 • Benkhoff, J., Murakami, G., Baumjohann, W. et al. (2021) BepiColombo -
565 Mission Overview and Science Goals. Space Sci Rev 217, 90,
566 https://doi.org/10.1007/s11214-021-00861-4
567 • Bertotti, B., Comoretto, G., and Iess, L. (1993) Doppler Tracking of Spacecraft
568 with Multi-frequency Links. Astron. Astrophys. 269, 608, 1993
569 • Bertotti, B., and Giampieri G. (1998) Solar Coronal Plasma in Doppler
570 Measurements. Solar Physics, 178, 85-107, doi: 10.1023/A:1004938717700
571 • Bertotti, B., Iess, L., and Tortora, P. (2003). A test of general relativity using
572 radio links with the Cassini spacecraft. Nature, 425(6956), 374-376,
573 https://doi.org/10.1038/nature01997
574 • Besse, S., Vallat, C., Barthelemy, M., Coia, D., Costa, M., De Marchi, G., et al.
575 (2018) ESA's Planetary Science Archive: Preserve and present reliable
576 scientific data sets. Planetary and Space Science, 150, 131–140,

https://doi.org/10.1016/j.pss.2017.07.013

- Brueckner, G. E., et al. (1995) The Large Angle Spectroscopic Coronagraph (LASCO). Solar Physics, 162:357–402, https://doi.org/10.1007/BF00733434
- Cappuccio, P., Imamura, T., Doria, I., Chiba, S., di Stefano, I., Shiota, D., Asmar, S., Iess, L. (2024) Probing solar wind velocity from simultaneous superior solar conjunction radio science experiments of BepiColombo and Akatsuki missions. Monthly Notices of the Royal Astronomical Society, 533(2), pp 1560–1567, https://doi.org/10.1093/mnras/stae1929
- Chiba, S., Imamura, T., Tokumaru, M., et al. (2022) Observation of the Solar Corona Using Radio Scintillation with the Akatsuki Spacecraft: Difference Between Fast and Slow Wind. Solar Physics 297:34, https://doi.org/10.1007/s11207-022-01968-9
- Coles, W.A., and Harmon, J.K., (1989) Propagation Observations of the Solar wind near the Sun. The Astrophysical Journal, 337 pp. 1023-1034
- Cranmer, S. R. (2004) New insights into solar wind physics from SOHO. arXiv preprint astro-ph/0409260, https://doi.org/10.48550/arXiv.astro-ph/0409260

- Cranmer, S.R. (2012) Self-Consistent Models of the Solar Wind. Space Science Reviews, 172:145–156, https://doi.org/10.1007/s11214-010-9674-7
- Cranmer, S.R., and Winebarger, A.R. (2019) The Properties of the Solar Corona and Its Connection to the Solar Wind. Astron. Astrophys., 57:1–30, https://doi.org/10.1146/annurev-astro-091918-104416
- Domingo, V., Fleck, B., and Poland, A.I. (1995) The SOHO mission: an overview. Solar Physics, 162(1), 1-37, https://doi.org/10.1007/BF00733425
- Doria, I., Cappuccio, P., Durante, D., di Stefano, I., Bernacchia, D., Lasagni Manghi, R., et al. (2025) BepiColombo calibrated plasma data [Dataset]. Zenodo. https://doi.org/10.5281/zenodo.17813314
- Doria, I., Cappuccio, P., Iess, L., Characterizing the solar-coronal electron density with BepiColombo multi-frequency range measurements. Earth, Planets and Space, submitted
- Dulk, G.A., and McLean, D.J. (1978) Coronal magnetic fields. Solar Physics, 57, 279, https://doi.org/10.1007/BF00160102
- Eberhart, R., Kennedy J. (1995) A new optimizer using particle swarm theory.

609 Proceedings of the 6th international symposium on micro machine and human
610 science, pp 39–43, Nagoya, Japan, Mar 13–16, 1995
611 • Efimov, A.I., Chashei, I.V., Bird, M.K., Samoznaev, L.N., and Plettemeier, D.
612 (2005) Turbulence in the inner solar wind determined from frequency
613 fluctuations of the downlink signals from the ULYSSES and GALILEO
614 spacecraft. Astronomy reports, 49(6), 485-494,
615 https://doi.org/10.1134/1.1941491
616 • Fremouw, E.J., Leadabrand, R.L., Livingstone, R.C., Cousin, M.D., Rino, C.L.,
617 Fair, B.C., Long, R.A. (1978) Early results from the DNA Wideband satellite
618 experiment – complex signal analysis. Radio Sci. 13(1), pp. 167-187, doi:
619 10.1029/RS013i001p00167
620 • Goldstein, M.L., and Roberts, D.A. (1995) Magnetohydrodynamics Turbulence
621 in the Solar Wind. Annu. Rev. Astron. Astrophys., 33:283-325,
622 https://doi.org/10.1063/1.873680
623 • Hara, H. (2018) Coronal Heating: Issues Revealed from Hinode Observations.
624 In: Shimizu, T., Imada, S., Kubo, M. (eds) First Ten Years of Hinode Solar On-

625 Orbit Observatory. Astrophysics and Space Science Library, vol 449. Springer,
626 Singapore, 2018
627 • Ho, C.M. (2010) Solar corona and solar wind effects. DSN
628 Telecommunications Link Design Handbook, 810-005, 106, Rev. B
629 • Iess, L., Asmar S.W., Cappuccio P., et al. (2021) Gravity, Geodesy and
630 Fundamental Physics with BepiColombo's MORE Investigation. Space Sci Rev
631 217, 21, https://doi.org/10.1007/s11214-021-00800-3
632 • Iijima, H., Matsumoto, T., Hotta, H., and Imada, S., (2023) A Comprehensive
633 Simulation of Solar Wind Formation from the Solar Interior: Significant Cross-
634 field Energy Transport by Interchange Reconnection near the Sun. The
635 Astrophysical Journal Letters, 951(2), L47, doi: 10.3847/2041-8213/acdde0
636 • Imamura, T., Noguchi, K., Nabatov, A., et al. (2005) Phase scintillation
637 observation during coronal sounding experiments with NOZOMI spacecraft.
638 Astronomy and Astrophysics, 439, 1165, https://doi.org/10.1051/0004-
639 6361:20042614
640 • Imamura, T., et al. (2014) Outflow structure of the quiet Sun corona probed by

641 spacecraft radio scintillations in strong scattering. The Astrophysical Journal,
642 788(2), 117, doi: 10.1088/0004-637X/788/2/117
643 • Kennedy, J., and Eberhart, R. (1995) Particle swarm optimization (PSO). In
644 Proc. IEEE international conference on neural networks, Perth, Australia (Vol.
645 4, No. 1, pp. 1942-1948), IEEE Service Center, Piscataway, NJ, November
646 1995
647 • Kosugi, T., Matsuzaki, K., Sakao, T., Shimizu, T., Sone, Y., Tachikawa, S., ...
648 and Golub, L. (2007) The Hinode (Solar-B) mission: an overview. Solar
649 Physics, 243(1), 3-17, https://doi.org/10.1007/s11207-007-9014-6
650 • Lasagni Manghi, R., Bernacchia, D., Gomez Casajus, L., Zannoni, M., Tortora,
651 P., Martellucci, A., et al. (2023) Tropospheric delay calibration system
652 performance during the first two BepiColombo solar conjunctions. Radio
653 Science, 58, e2022RS007614, doi: 10.1029/2022RS007614
654 • Lemen, J.R., Title, A.M., Akin, D.J. et al. (2012) The Atmospheric Imaging
655 Assembly (AIA) on the Solar Dynamics Observatory (SDO). Solar Physics,
656 275, 17–40, https://doi.org/10.1007/s11207-011-9776-8

- Manoharan, P. K., and Salter, C. J. (2025) Arecibo Multifrequency IPS Observations: Solar-Wind Density Turbulence Scale Sizes and Their Anisotropy. Solar Physics, 300(4), 40, https://doi.org/10.1007/s11207-025-02445-9
- Marsch, E. (2012) Helios: evolution of distribution functions 0.3–1 AU. Space science reviews, 172(1), 23-39, https://doi.org/10.1007/s11214-010-9734-z
- Marsden, R. G. (1996) A summary of solar wind observations at high latitudes: Ulysses. Space Science Reviews, 78(1), 67-72, https://doi.org/10.1007/BF00170793
- Pesnell, W. D., Thompson, B. J., and Chamberlin, P. C. (2012) The solar dynamics observatory (SDO). Solar Physics, 275:3–15, doi: 10.1007/s11207-011-9841-3
- Priyadarshi, S. (2015) A review of ionospheric scintillation models. Surveys in geophysics, 36(2), 295-324, https://doi.org/10.1007/s10712-015-9319-1
- Raja, K.S., Subramanian, P., Ingale, M., Ramesh, R. (2019) Dissipation scale lengths of solar wind turbulence. The Astrophysical Journal, 872, 77,

673 10.3847/1538-4357/aafd33

674 • Raouafi, N. E., Matteini, L., Squire, J., Badman, S. T., Velli, M., Klein, K.
675 G., ... and Woolley, T. (2023) Parker solar probe: Four years of discoveries at
676 solar cycle minimum. Space Science Reviews, 219(1), 8,
677 https://doi.org/10.1007/s11214-023-00952-4

678 • Richie-Halford, A.C., Iess, L., Tortora, P., Armstrong, J.W., Asmar, S.W.,
679 Woo, R., Habbal, S.R., and Morgan, H. (2009) Space-time localization of inner
680 heliospheric plasma turbulence using multiple spacecraft radio links. Space
681 Weather, 7, S12003, https://doi.org/10.1029/2009SW000499

682 • Sadykov, V.M., Kosovichev, A.G., Kitiashvili, I.N., and Kerr, G.S. (2020)
683 Response of SDO/HMI observables to heating of the solar atmosphere by
684 precipitating high-energy electrons. The Astrophysical Journal, 893(1), 24, doi:
685 10.3847/1538-4357/ab7b6a

686 • Sakurai, T., Spangler, S.R., and Armstrong, J.W. (1992) Very long baseline
687 interferometer measurements of plasma turbulence in the solar wind. Journal of
688 Geophysical Research: Space Physics, 97(A11), 17141-17151,

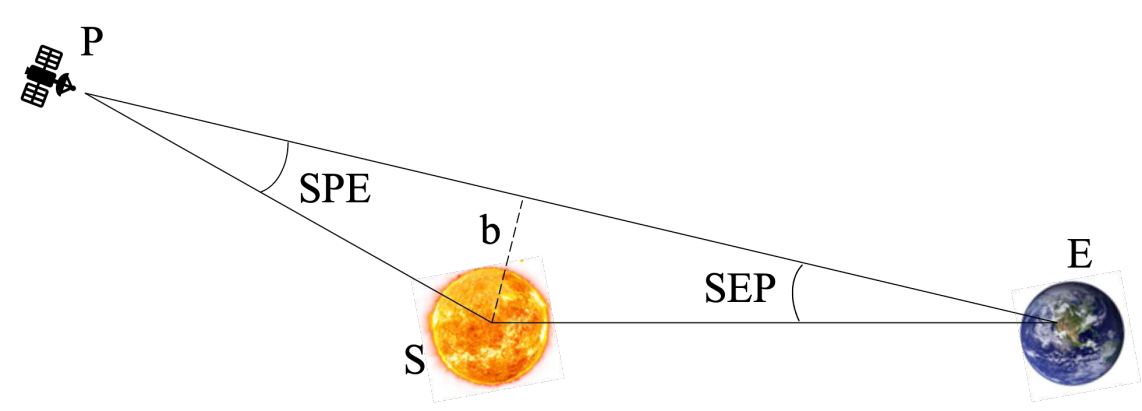
https://doi.org/10.1029/92JA01551

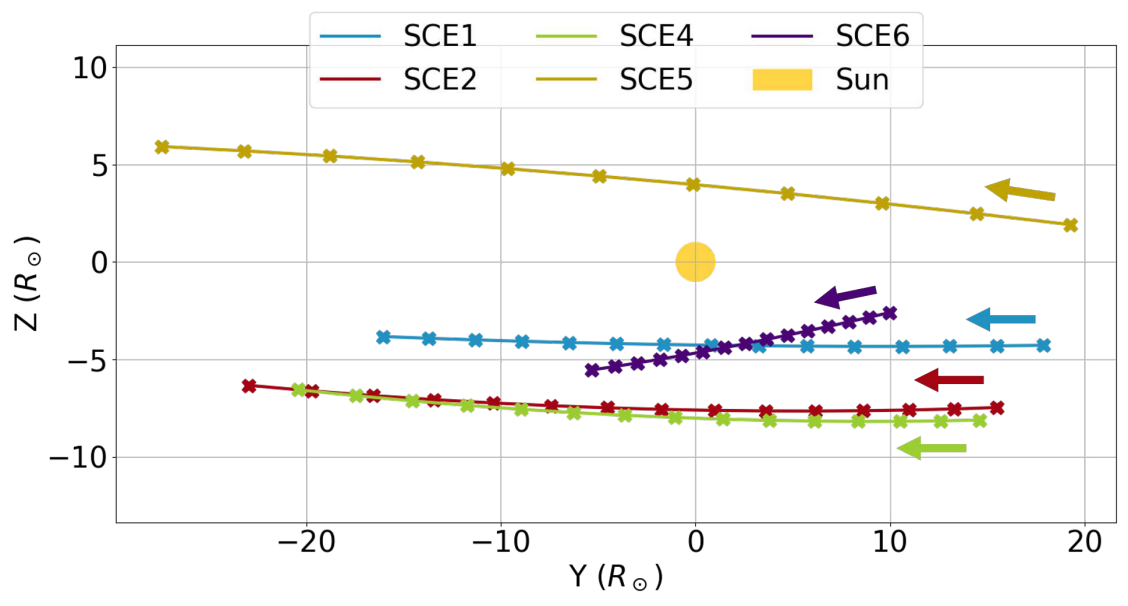
- Scott, S. L., W. A. Coles and G. Bourgois (1983) Solar wind observations near the sun using interplanetary scintillation. Astronomy and Astrophysics 123, 207-215
- Shoda, M., Suzuki, T.K., Asgari-Targhi, M., and Yokoyama, T. (2019) Three-dimensional Simulation of the Fast Solar Wind Driven by Compressible Magnetohydrodynamic Turbulence. The Astrophysical Journal Letters, 880:L2, doi: 10.3847/2041-8213/ab2b45
- Spangler, R.S., et al. (2002) Very Long Baseline Interferometer measurements of turbulence in the inner solar wind. Astronomy and Astrophysics 384, 654-665, https://doi.org/10.1051/0004-6361:20020028
- Stakhiv, M., Lepri, S.T., Landi, E., Tracy, P., and Zurbuchen, T.H. (2016) On solar wind origin and acceleration: Measurements from ACE. The Astrophysical Journal, 829(2), 117, doi: 10.3847/0004-637X/829/2/117
- Stoica, P., and Moses, R. (2005) Spectral Analysis of Signals. Prentice Hall, Upper Saddle River, New Jersey

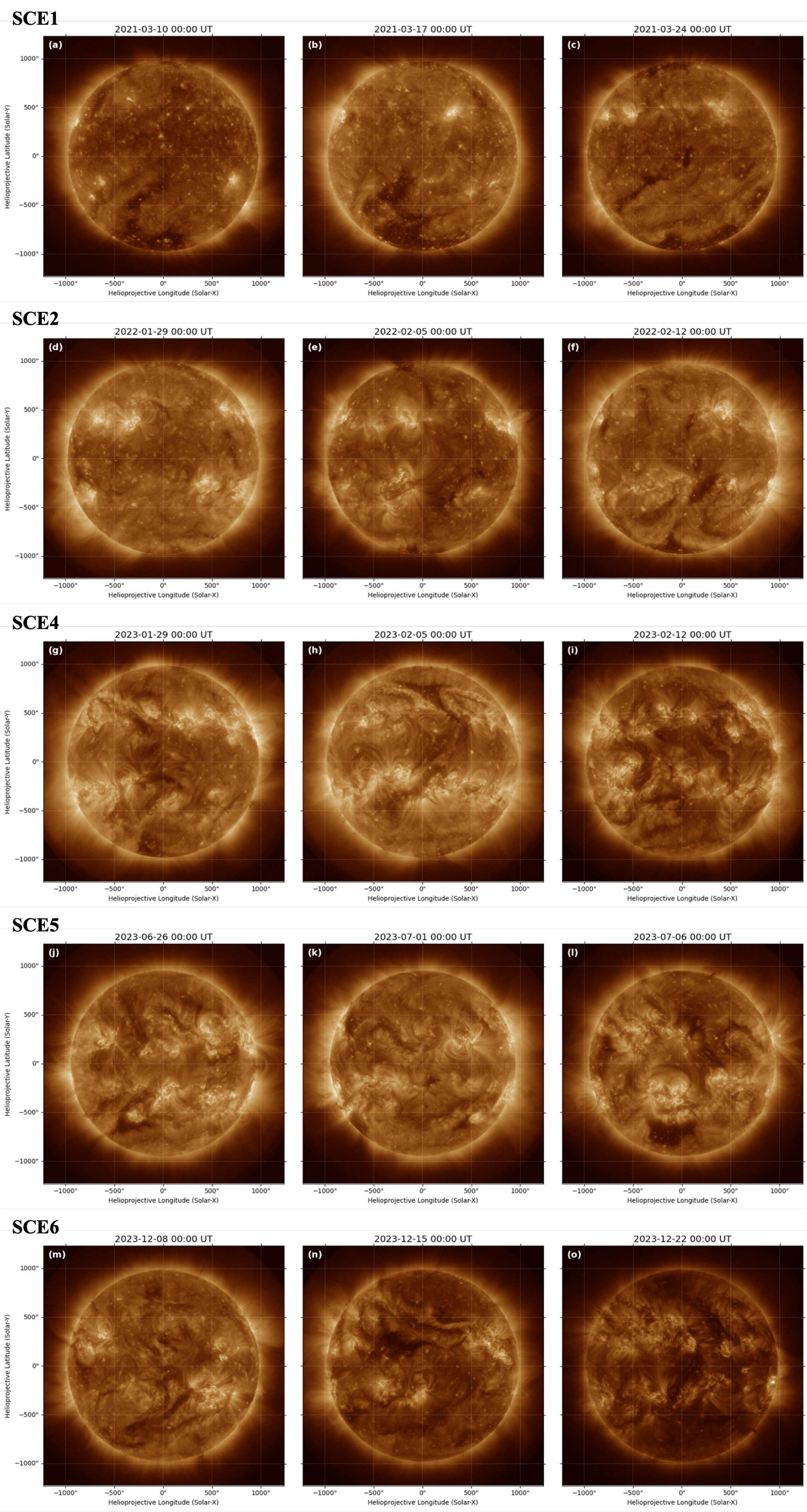
- Suzuki, T.K., and Inutsuka, S.-i. (2005) Making the corona and the fast solar wind: a self-consistent simulation for the low-frequency Alfvén waves from the photosphere to 0.3 AU. The Astrophysical Journal Letters, 632: L49, doi: 10.1086/497536
- Tokumaru, M., Mori, H., Tanaka, T., Kondo, T., Takaba, H., and Koyama, Y. (1991) Solar wind near the sun observed with interplanetary scintillation using three microwave frequencies. Journal of geomagnetism and geoelectricity, 43(8), 619-630, https://doi.org/10.5636/jgg.43.619
- Tortora, P., Iess, L., et al. (2004) Precise Cassini Navigation During Solar Conjunctions Through Multifrequency Plasma Calibrations. Journal of Guidance, Control and Dynamics 27:2, 251-257, https://dx.doi.org/10.2514/1.997
- Tyler, G.L., et al. (1977) The Viking Solar Corona Experiment. Journal of Geophysical Research 82, no. 28, https://doi.org/10.1029/JS082i028p04335
- Viall, N.M., and Borovsky, J.E. (2020) Nine outstanding questions of solar wind physics. Journal of Geophysical Research: Space Physics, 125,

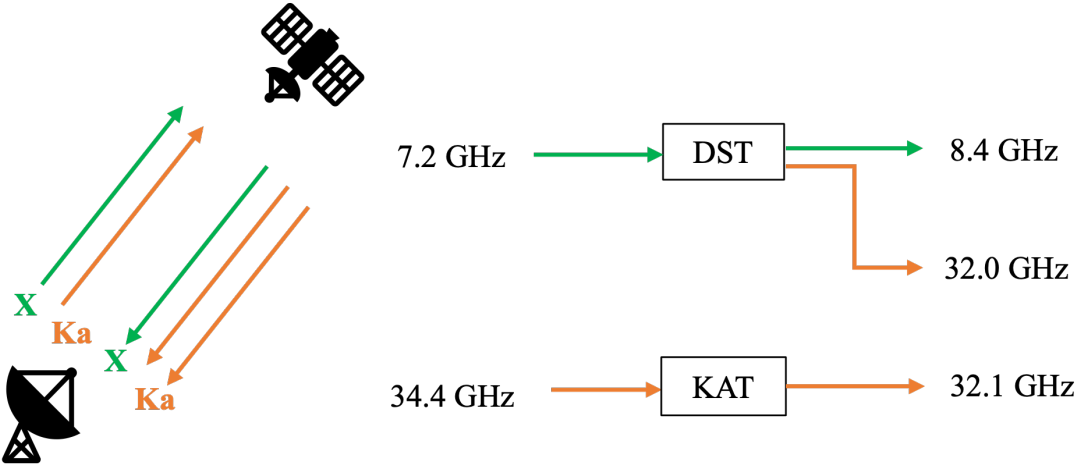
e2018JA026005, doi: 10.1029/2018JA026005

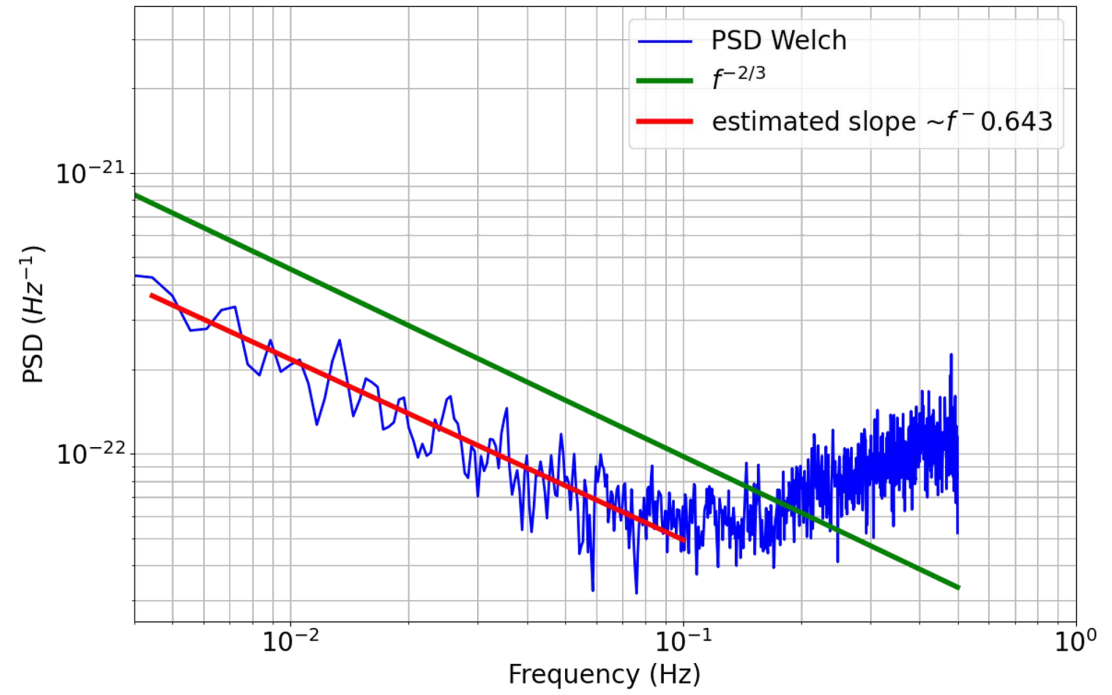
- Withers, P. (2010) Prediction of uncertainties in atmospheric properties measured by radio occultation experiments. Advances in Space Research, 46(1), 58-73, doi: 10.1016/j.asr.2010.03.004
- Woo, R. and Armstrong, J.W. (1979) Spacecraft Radio Scattering Observations of the Power Spectrum of Electron Density Fluctuations in the Solar Wind. Journal of Geophysical Research 84, no. Al2, https://doi.org/10.1029/JA084iA12p07288
- Zank, G.P., Zhao, L.L., Adhikari, L., Telloni, D., Kasper, J.C., and Bale, S.D. (2021) Turbulence transport in the solar corona: Theory, modeling, and Parker Solar Probe. Physics of Plasmas, 28(8), https://doi.org/10.1063/5.0055692

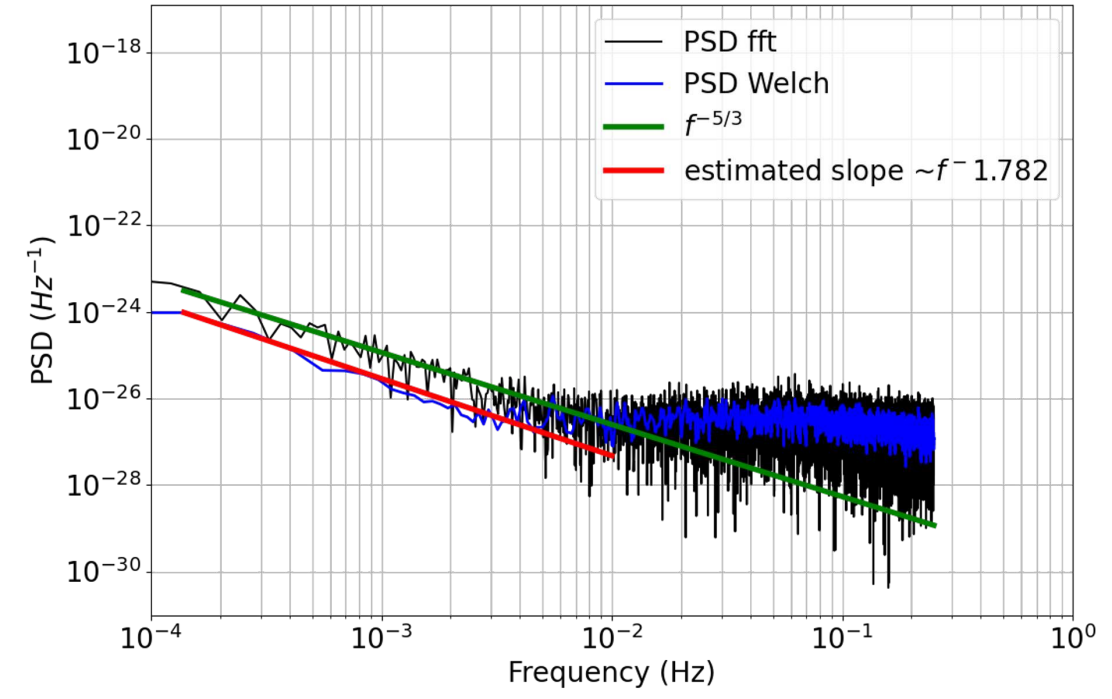

P
SPE
b
S
SEP
E

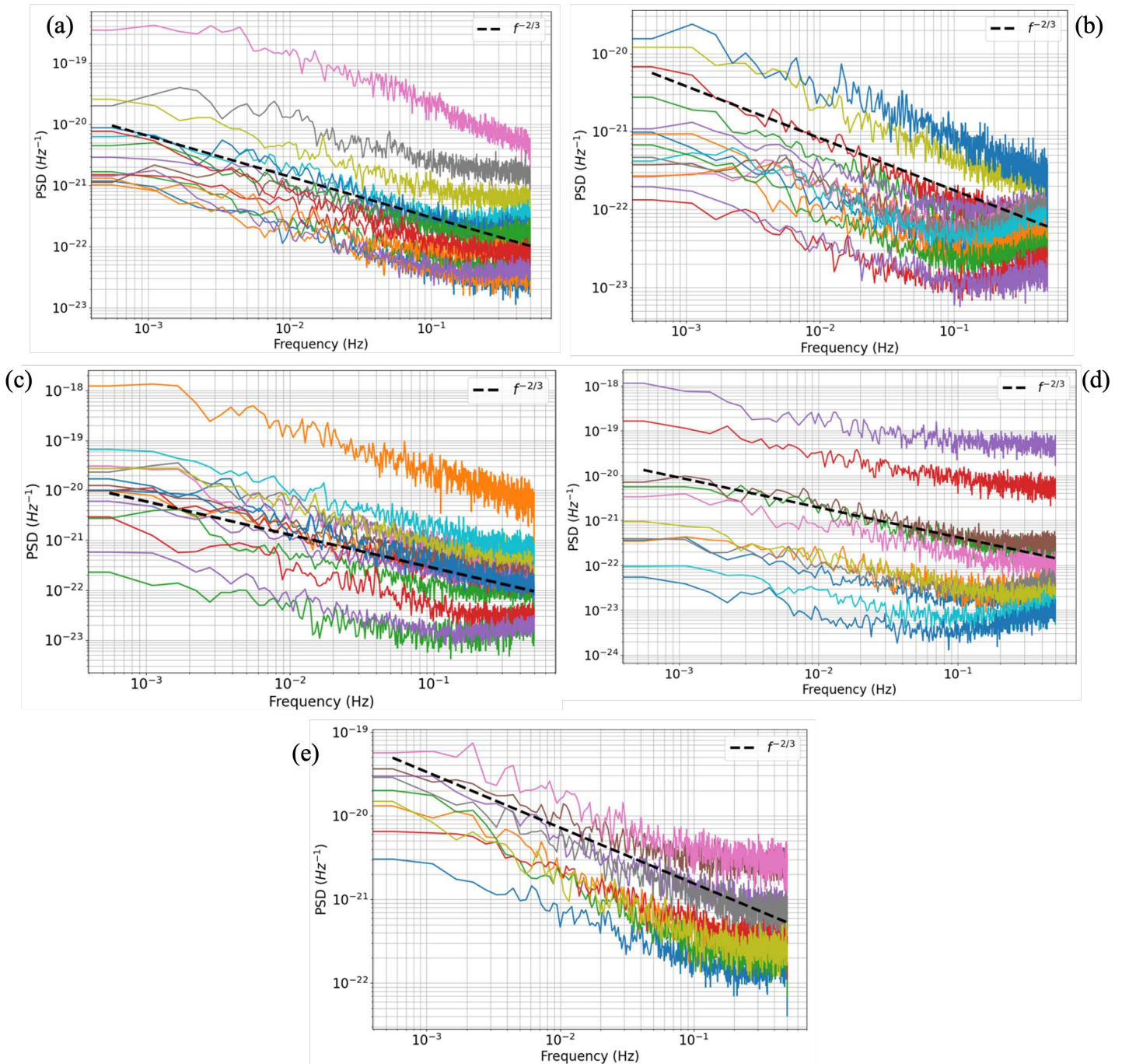

SCE1
SCE2
SCE4
SCE5
SCE6
Sun
10
5
0
−5
−10
Z ($R_\odot$)
−20
−10
0
10
20
Y ($R_\odot$)

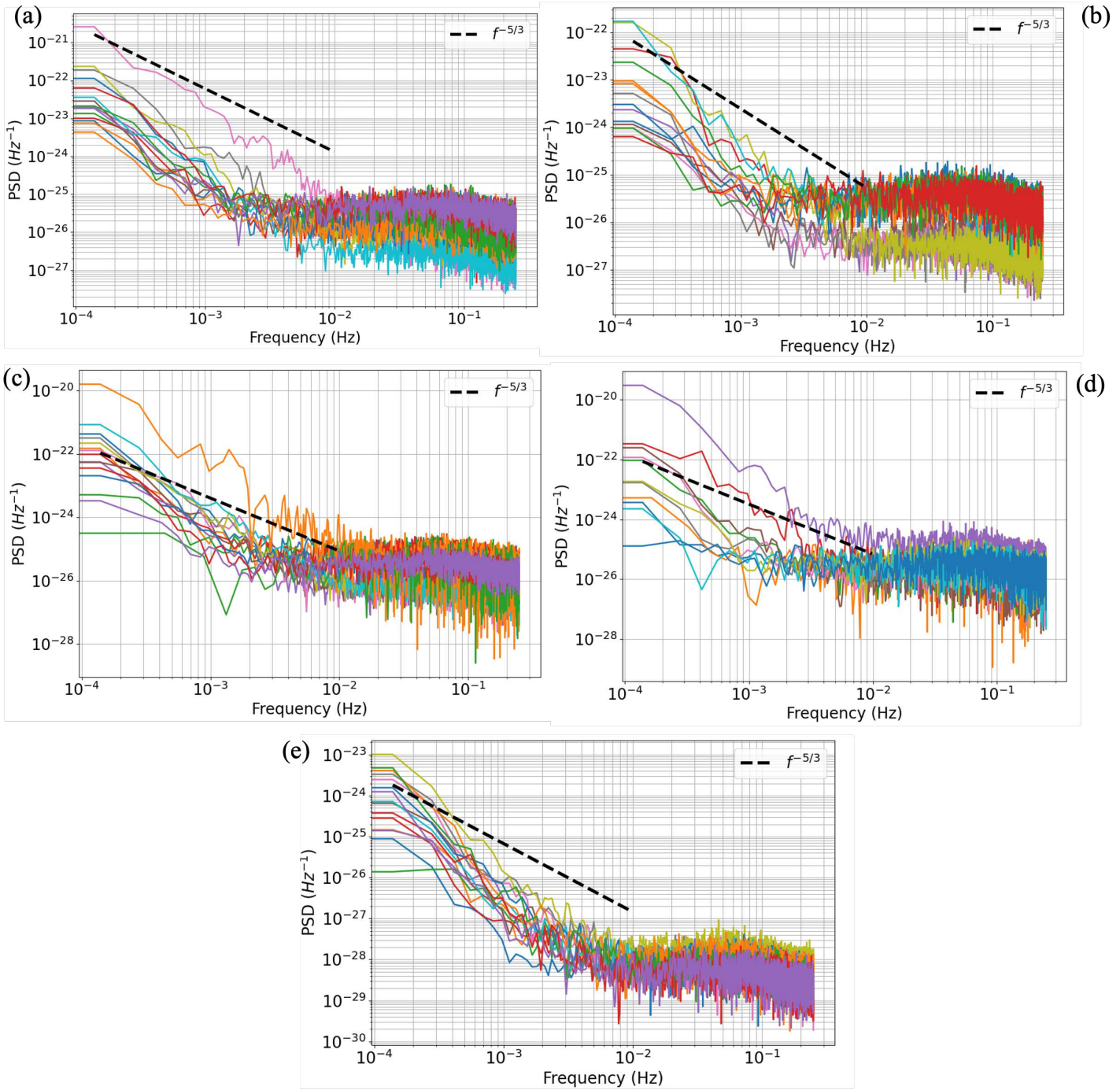

SCE1
2021-03-10 00:00 UT
2021-03-17 00:00 UT
2021-03-24 00:00 UT
(a)
(b)
(c)
SCE2
2022-01-29 00:00 UT
2022-02-05 00:00 UT
2022-02-12 00:00 UT
(d)
(e)
(f)
SCE4
2023-01-29 00:00 UT
2023-02-05 00:00 UT
2023-02-12 00:00 UT
(g)
(h)
(i)
SCE5
2023-06-26 00:00 UT
2023-07-01 00:00 UT
2023-07-06 00:00 UT
(j)
(k)
(l)
SCE6
2023-12-08 00:00 UT
2023-12-15 00:00 UT
2023-12-22 00:00 UT
(m)
(n)
(o)
Helioprojective Latitude (Solar-Y)
Helioprojective Longitude (Solar-X)
1000"
500"
0"
−500"
−1000"

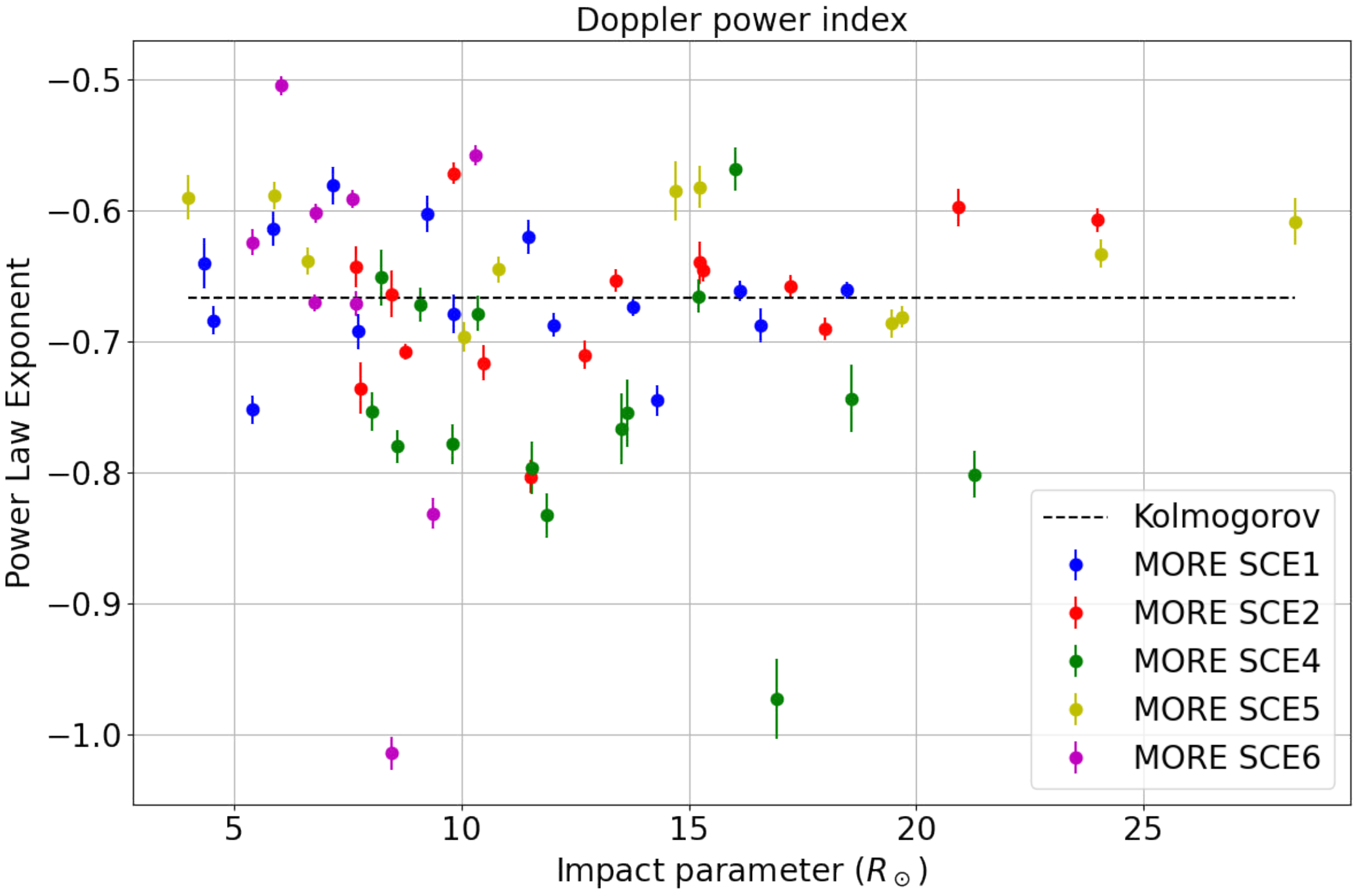

X
Ka
X
Ka
7.2 GHz
DST
8.4 GHz
32.0 GHz
34.4 GHz
KAT
32.1 GHz

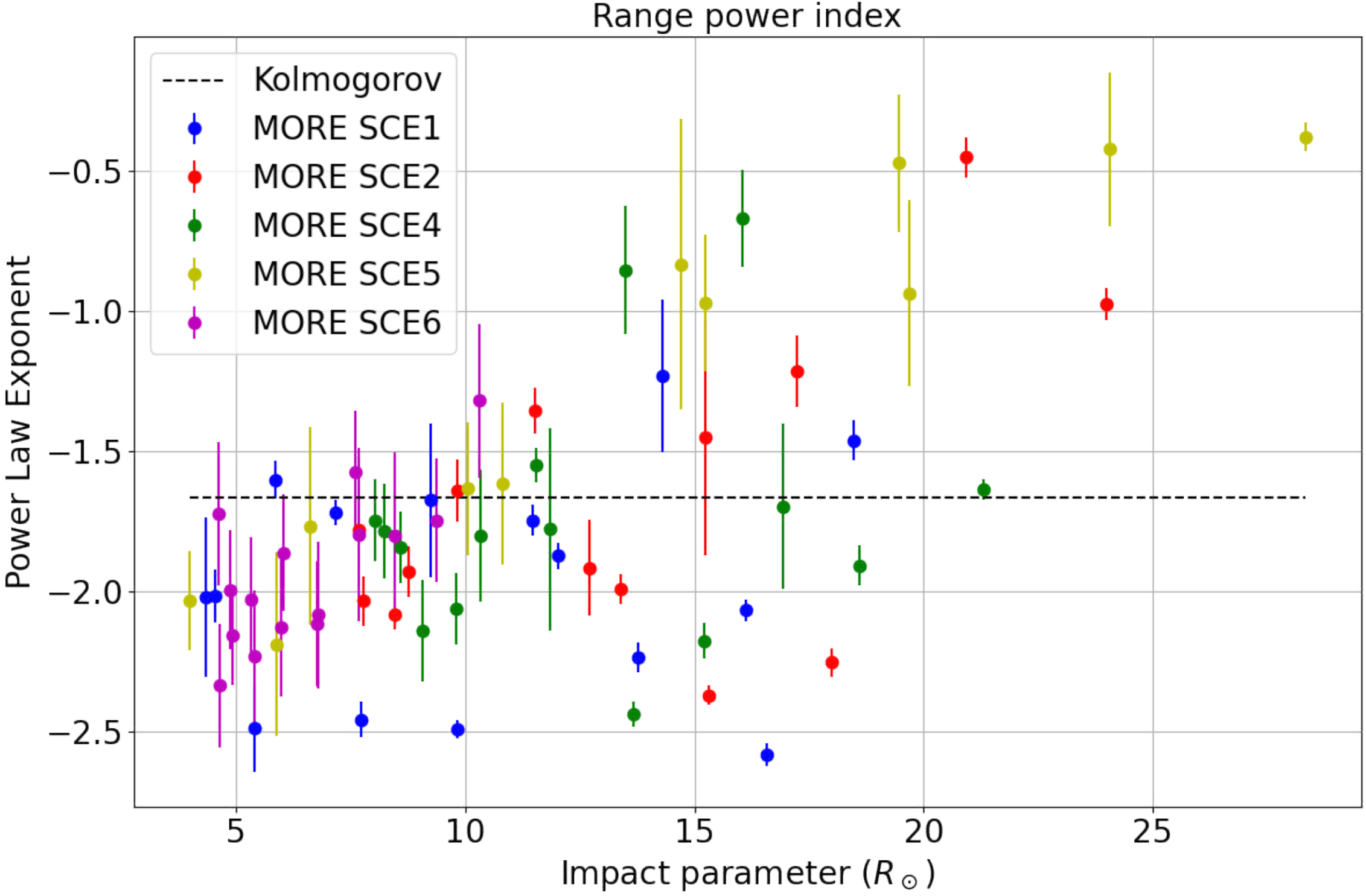

PSD Welch
$f^{-2/3}$
estimated slope $\sim f^{-}$ 0.643
10^{-21}
10^{-22}
PSD (Hz^{-1})
10^{-2}
10^{-1}
10^{0}
Frequency (Hz)

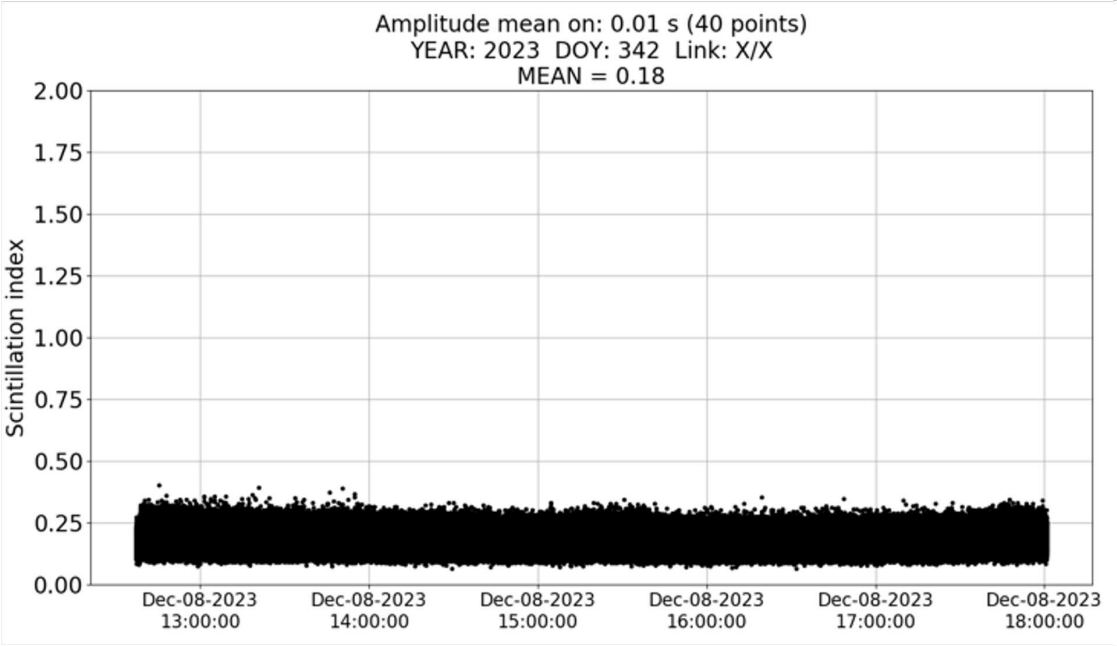

PSD fft
PSD Welch
$f^{-5/3}$
estimated slope $\sim f^{-}$ 1.782
10^{-18}
10^{-20}
10^{-22}
10^{-24}
10^{-26}
10^{-28}
10^{-30}
PSD (Hz^{-1})
10^{-4}
10^{-3}
10^{-2}
10^{-1}
10^{0}
Frequency (Hz)

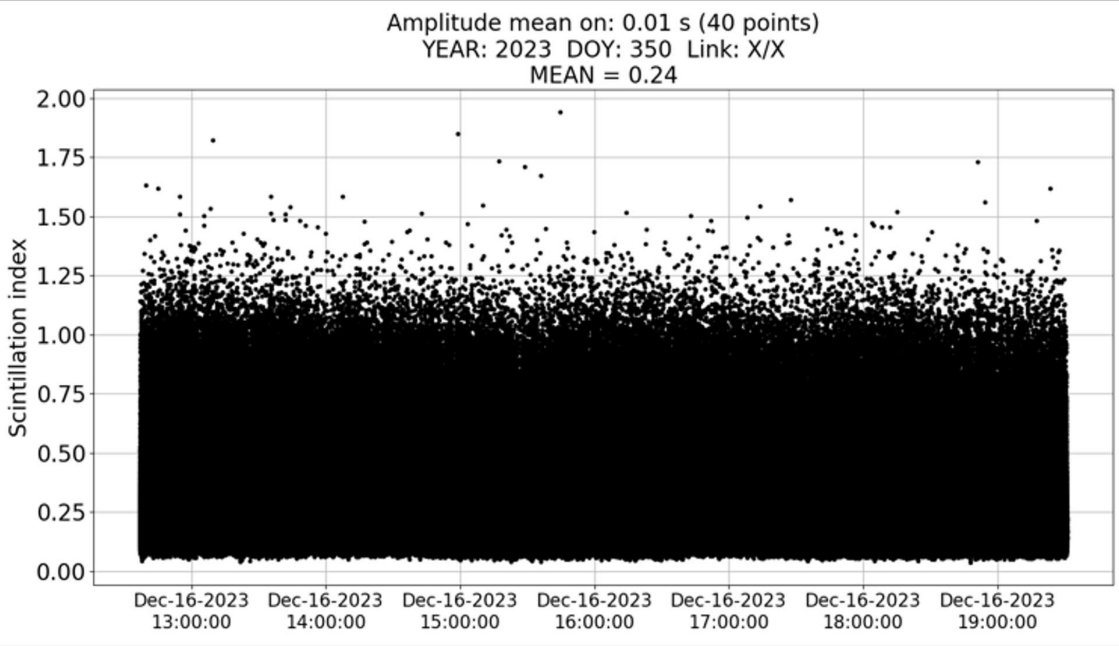

(a)
(b)
(c)
(d)
(e)
$f^{-2/3}$
PSD (Hz^{-1})
Frequency (Hz)

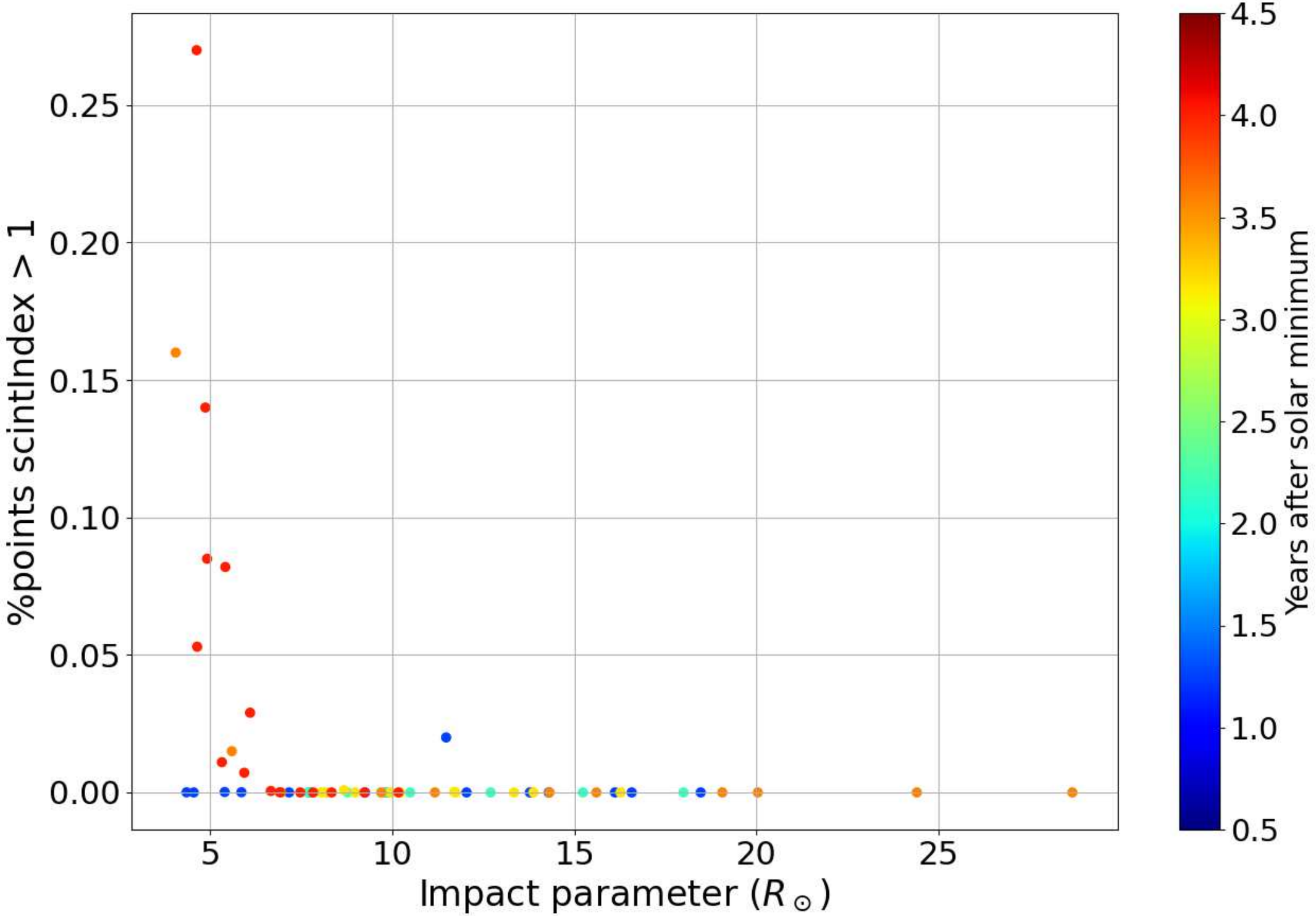

(a)
(b)
(c)
(d)
(e)
$f^{-5/3}$
PSD (Hz^{-1})
Frequency (Hz)

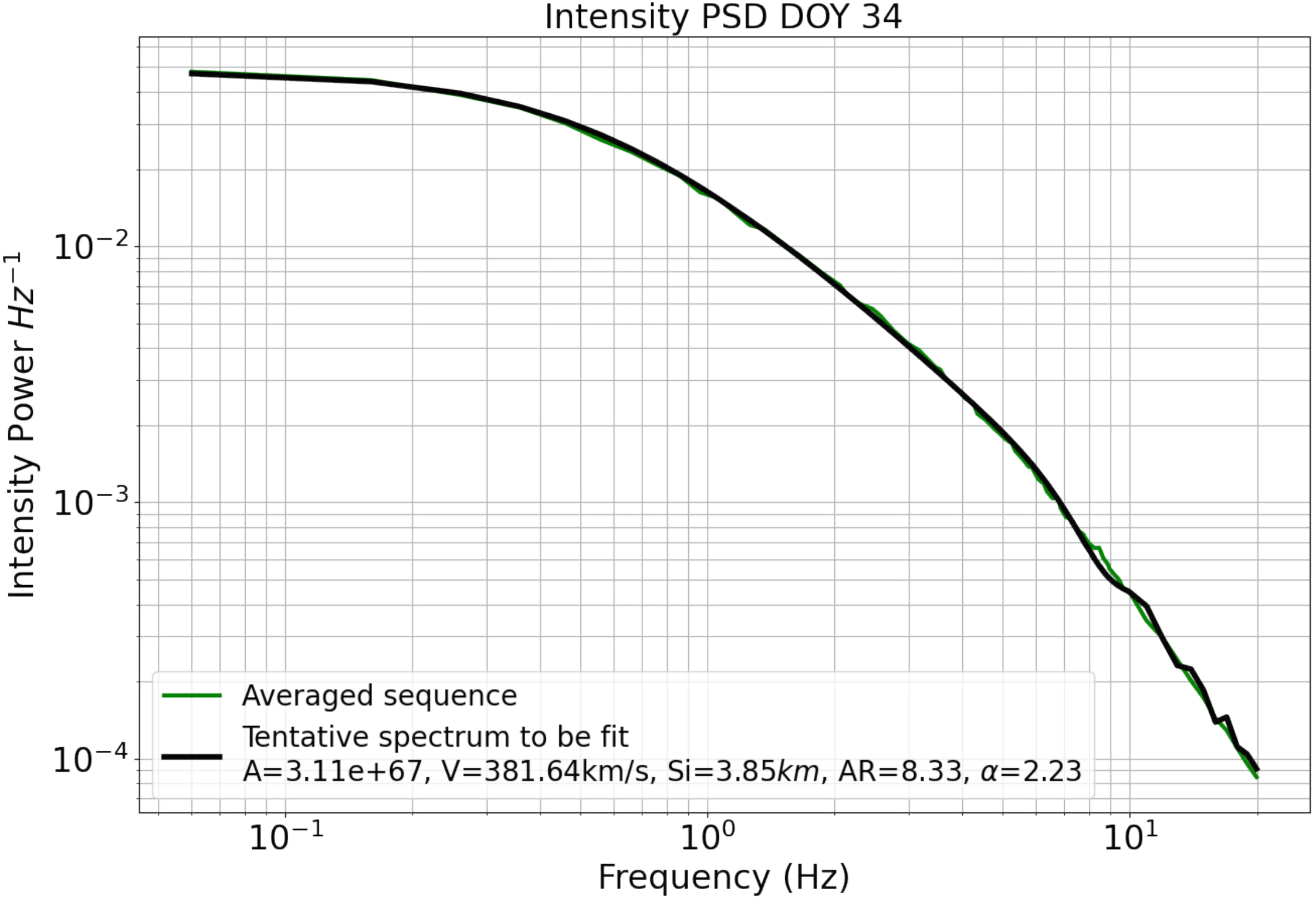

Doppler power index
−0.5
−0.6
−0.7
−0.8
−0.9
−1.0
Power Law Exponent
5
10
15
20
25
Impact parameter ($R_\odot$)
Kolmogorov
MORE SCE1
MORE SCE2
MORE SCE4
MORE SCE5
MORE SCE6


Range power index
Kolmogorov
MORE SCE1
MORE SCE2
MORE SCE4
MORE SCE5
MORE SCE6
−0.5
−1.0
−1.5
−2.0
−2.5
Power Law Exponent
5
10
15
20
25
Impact parameter ($R_\odot$)

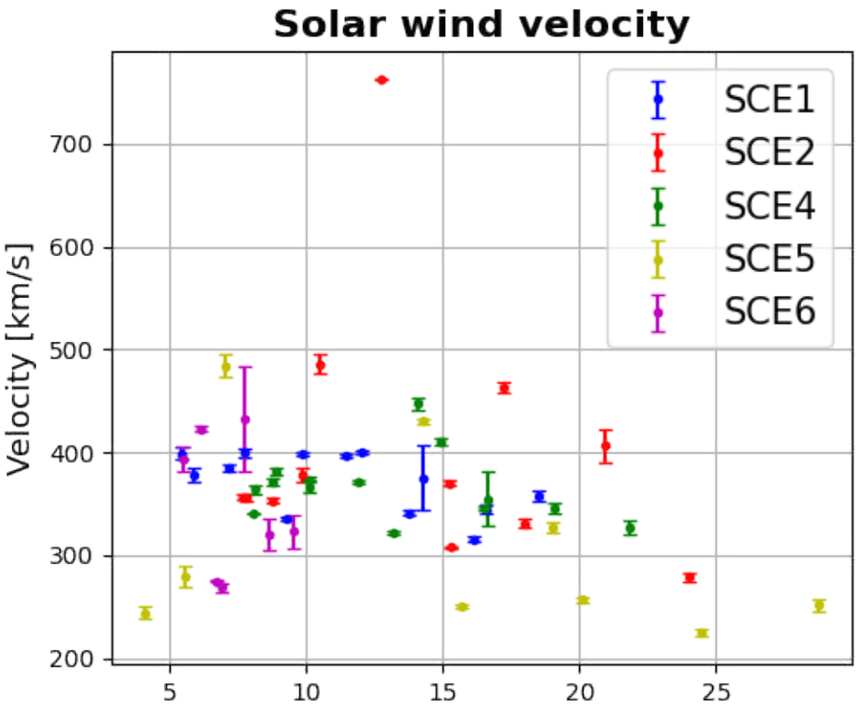

Amplitude mean on: 0.01 s (40 points)
YEAR: 2023 DOY: 342 Link: X/X
MEAN = 0.18
Scintillation index
2.00
1.75
1.50
1.25
1.00
0.75
0.50
0.25
0.00
Dec-08-2023 13:00:00
Dec-08-2023 14:00:00
Dec-08-2023 15:00:00
Dec-08-2023 16:00:00
Dec-08-2023 17:00:00
Dec-08-2023 18:00:00

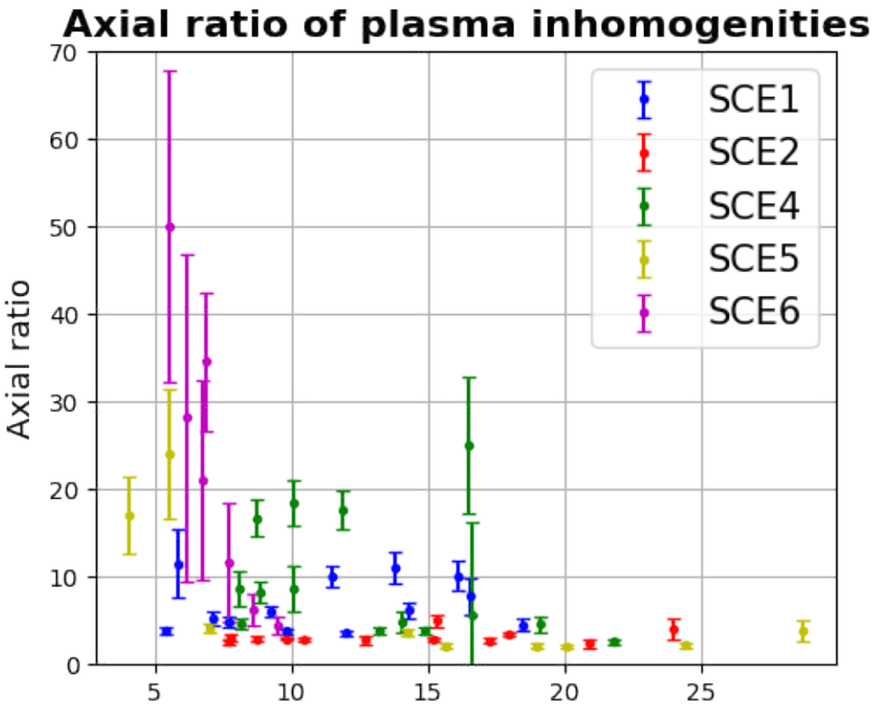

Amplitude mean on: 0.01 s (40 points)
YEAR: 2023 DOY: 350 Link: X/X
MEAN = 0.24
Scintillation index
2.00
1.75
1.50
1.25
1.00
0.75
0.50
0.25
0.00
Dec-16-2023 13:00:00
Dec-16-2023 14:00:00
Dec-16-2023 15:00:00
Dec-16-2023 16:00:00
Dec-16-2023 17:00:00
Dec-16-2023 18:00:00
Dec-16-2023 19:00:00

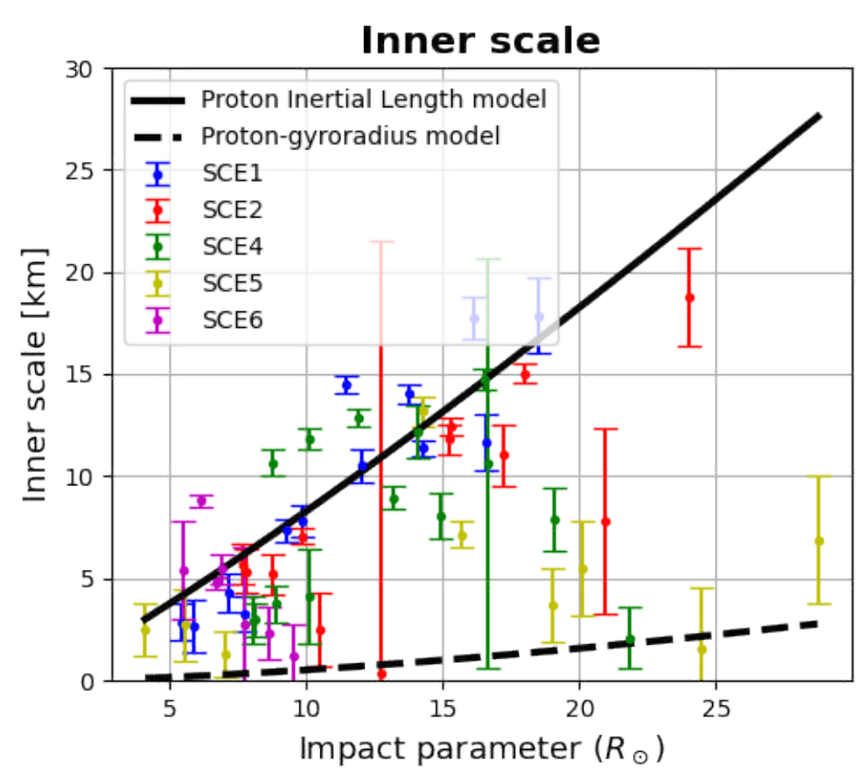

%points scintIndex > 1
0.25
0.20
0.15
0.10
0.05
0.00
5
10
15
20
25
Impact parameter ($R_\odot$)
4.5
4.0
3.5
3.0
2.5
2.0
1.5
1.0
0.5
Years after solar minimum

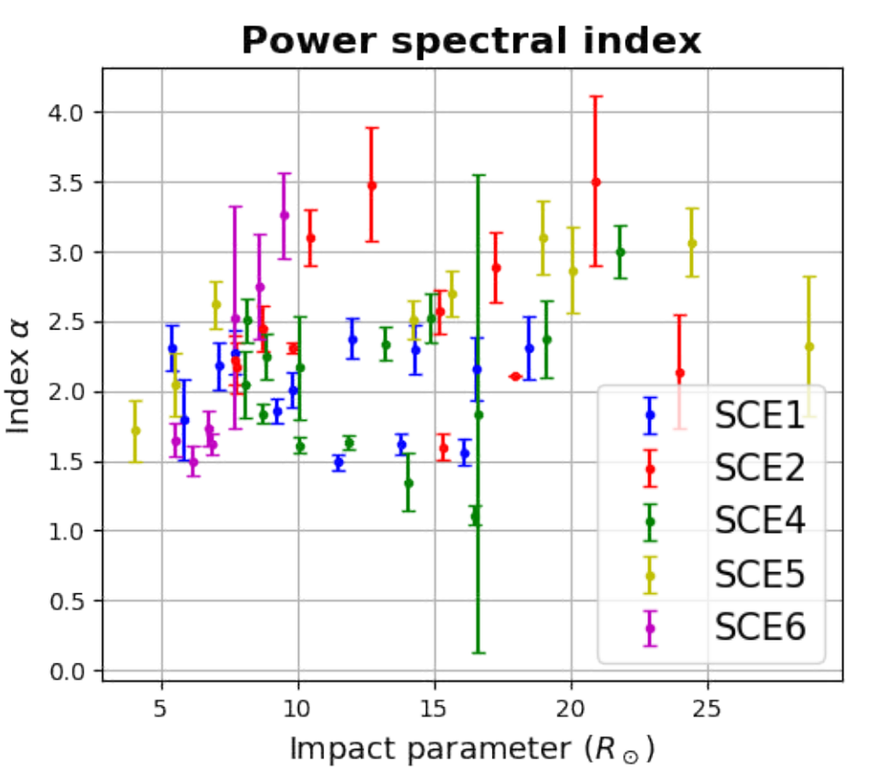

Intensity PSD DOY 34
Intensity Power Hz^{-1}
10^{-2}
10^{-3}
10^{-4}
10^{-1}
10^{0}
10^{1}
Frequency (Hz)
Averaged sequence
Tentative spectrum to be fit
A=3.11e+67, V=381.64km/s, Si=3.85km, AR=8.33, α=2.23

Solar wind parameters vs impact parameter









Supplementary Files

This is a list of supplementary files associated with this preprint. Click to download.

- Graphicalabstract.png